CHEMISTRY OF MATERIALS

pubs.acs.org/cm

Article

Material Dynamics of Manganese-Based Oxychlorides for Oxygen Evolution Reaction in Acid

Ruihan Li, Dennis Nordlund, and Linsey C. Seitz*

Cite This: *Chem. Mater.* 2024, 36, 1299−1307

Read Online

ACCESS | Metrics & More | Article Recommendations | Supporting Information

ABSTRACT: Earth-abundant manganese-based oxides have emerged as promising alternatives to noble-metal-based catalysts for the oxygen evolution reaction (OER) in acidic conditions; however, their inferior activity and stability present critical challenges for the sustainable production of hydrogen via water electrolysis. Moving beyond oxides, heteroanionic materials, which incorporate anions with lower electronegativity than oxygen, have shown potential for improving the OER performance, but a detailed understanding of the underlying mechanisms is lacking. Here, we investigate manganese-based oxychlorides ($Mn_8O_{10}Cl_3$ and $FeMn_7O_{10}Cl_3$) that exhibit excellent activity and stability for acidic OER to elucidate material property dynamics and correlate them with OER behaviors. Our rigorous electrochemical stability testing reveals that the high operating potential mitigates Mn dissolution over prolonged exposure to the OER conditions. Through a combination of *ex situ* and *in situ* surface and bulk-sensitive X-ray spectroscopy analyses, we observe a trade-off between increasing Mn valence and maintaining structural integrity, which results in dynamic bond length changes within the [$MnCl_6$] octahedra during the activation and degradation processes of these oxychloride catalysts. This study provides insights into the fundamental relationships between the chemical, electronic, and geometric properties of the catalysts and their electrocatalytic outcomes.

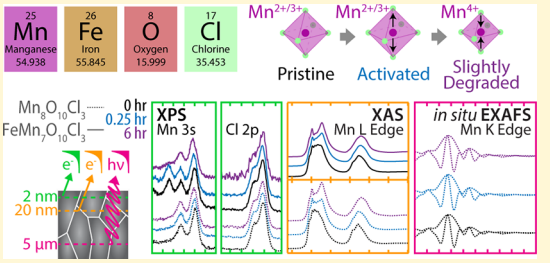

INTRODUCTION

As the threat of climate change grows, electrocatalytic conversion is seen as a crucial technology for producing important fuels and chemicals as well as reducing our reliance on fossil fuels. Hydrogen generated through water electrolysis is an increasingly attractive option for heavy freight and seasonal energy storage, as well as for significantly reducing CO_2 emissions in hydrogen-intensive processes such as ammonia synthesis. However, the anodic oxygen evolution reaction (OER) poses challenges in terms of cost and energy efficiency, as the electrocatalytic materials that are both active and stable under oxidizing conditions are limited to transition metal-based oxides.[1−5]

To address this challenge, heteroanionic materials (HAMs) have been explored to widen the scope of possible material-tuning parameters. HAMs are compounds where the anion sublattice consists of two or more anionic species (distinct from polyatomic ions (i.e., NO_3^-) where the entire ion behaves as a single unit).[6] By exchanging anions with electronegativities and charges different from those of O^{2-}, such as halide ions, the electronic structure of catalysts can be modified. For example, the presence of highly electronegative fluorine has been found to create electron-deficient active sites, enhancing electronic conductivity (i.e., amorphous $NiFe_2F_{4.4}O_{1.8}$[7]) or promoting surface oxygen vacancies (i.e., Sr_2CoO_3F[8]), which in turn improve OER performance. Density functional theory calculations have revealed that the incorporation of chlorine, which lies at a lower orbital energy, can upshift the O p-band center and enhance the activity of cobalt-based perovskite oxychlorides (Sr_2CoO_3Cl, $Sr_3Co_2O_5Cl_2$[9]). However, most efforts thus far have focused on Ni-, Fe-, and Co-based oxyhalides that are primarily used in alkaline conditions. In comparison, polymer electrolyte membrane water electrolysis offers advantages such as higher energy efficiency, faster system response, and a larger partial load range compared to their alkaline counterparts.[10−12] However, the highly acidic environment combined with high operating potentials necessitates the use of noble metals (i.e., Ir and Ru).[2,3,5,13−18] Given the high cost and insufficient reserves of these metals, it is crucial to develop cost-effective catalysts that reduce or eliminate the precious metal contents while preserving or even enhancing the performance.[19,20]

Manganese oxides have been proposed as potential catalyst materials for acidic OER due to a narrow thermodynamic stability window in low pH, but their activity still lags far behind that of noble-metal-based oxides. Recently, Mn-based oxyhalides including $MnFe_2F_{5.8}O_{1.1}$,[21] $Mn_8O_{10}Cl_3$, and $Mn_{7.5}O_{10}Br_3$[22] have shown excellent activity and stability for

Received: September 14, 2023
Revised: January 3, 2024
Accepted: January 4, 2024
Published: January 16, 2024

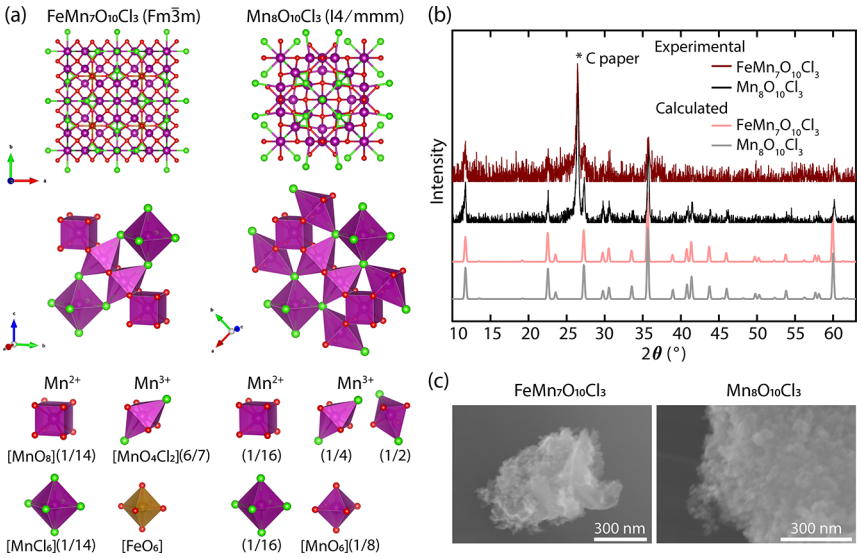

Figure 1. Pristine materials. (a) Structure of oxychlorides and isolated views of the component homoleptic and heteroleptic polyhedra. Polyhedral clusters show the arrangement of Mn building units; parentheses below each polyhedron indicate the fraction of metal found in that building unit. (b) GI-XRD of as-prepared electrodes. (c) SEM images of pristine $FeMn_7O_{10}Cl_3$ (left) and $Mn_8O_{10}Cl_3$ (right).

OER in strong acids. A separate work has demonstrated a correlation between the increased Mn oxidation state and low dissolution in acid for Mn-based oxides.[23] Furthermore, incorporating metals with higher electronegativity into oxides has also been predicted to improve stability. However, it is unclear whether this theory can be extended to Mn-based HAMs. More broadly, the effect of halogen incorporation on catalyst dynamics and structural changes of Mn-based HAMs that impact activation and degradation processes as well as short-term and long-term operation of these materials remains poorly understood.

Herein, we develop oxychlorides that utilize earth-abundant metals to correlate the catalytic performance of $Mn_8O_{10}Cl_3$ and $FeMn_7O_{10}Cl_3$ with their structural properties during long-term acidic OER. Combining electrochemical analysis, inductively coupled plasma mass spectrometry (ICP-MS), and *ex situ/in situ* X-ray absorption spectroscopy (XAS), we observe that highly oxidizing potentials mitigate Mn leaching during prolonged exposure to OER conditions, in parallel with structural evolution to an active phase featuring an elongated Mn−Cl bond and preserved $Mn^{2+/3+}$ mixed valence. We also identify material dynamics, which lead to a slight decrease in catalytic activity, corresponding with the shortening of the Mn−Cl bond and an increase in Mn^{4+} species. Our work provides a detailed analysis of the structural changes occurring in oxychlorides and elucidates the influence of chlorine on long-term activity and stability, highlighting the importance of both anion and cation engineering in designing non-noble metal electrocatalysts for acidic water oxidation.

RESULTS AND DISCUSSION

Pristine Oxychloride Materials. The oxychloride materials explored here, $Mn_8O_{10}Cl_3$ and $FeMn_7O_{10}Cl_3$, consist of mixed-valence $Mn^{2+/3+}$ and comprise both homoleptic and heteroleptic anion polyhedra around Mn centers, due to the differences in the anion size (Figure 1a). First, considering the structure of $Mn_8O_{10}Cl_3$, Mn^{2+} ions occupy cubic sites in oxide cubes [MnO_8] or octahedral sites in chloride octahedra [$MnCl_6$]; Mn^{3+} ions are distributed among three octahedral sites, including one undistorted oxide octahedron [MnO_6] and two highly distorted oxychloride octahedra [MnO_4Cl_2] due to the combined Jahn−Teller effect in Mn^{3+} and the presence of chlorine atoms.[24,25] This framework can be tuned by selectively substituting Fe^{3+} in the oxide octahedral sites. The mixed oxychloride $FeMn_7O_{10}Cl_3$ only contains one configuration of [MnO_4Cl_2] and exhibits cubic symmetry with the space group $Fm\bar{3}m$,[26] in contrast to the tetragonal $I4/mmm$[24] structure of $Mn_8O_{10}Cl_3$. The changes in the local structure due to partial Fe substitution enable identification of the building units that govern the catalytic activity and stability.

To enhance the signal from the catalyst materials compared to the substrate, X-ray diffractograms of electrodes were obtained at a shallow angle of 0.6° using grazing-incidence X-ray diffraction (GI-XRD, Figure 1b). Apart from the sharp peak at ∼26.5° which is attributed to the carbon paper substrate, all the characteristic peaks correspond to the cubic structure of $FeMn_7O_{10}Cl_3$[26] and the tetragonal structure of $Mn_8O_{10}Cl_3$,[24] respectively. Scanning electron microscopy (SEM, Figures 1c and S2) was employed to observe the morphology of as-prepared oxychloride materials, which form micrometer-sized aggregates composed of particles with sizes in the range of a few hundred nanometers.

Catalytic Activity and Stability. To monitor the catalytic performance primarily as a function of the operating potential and to investigate both the activation and deactivation processes, we employed a stability protocol that alternates long, constant potential holds (chronoamperometry, CA, Figure 3a) at 1.65 V versus RHE with briefly cycled potentials (cyclic voltammetry, CV, Figures 2 and S3). Additionally, *ex situ* ICP-MS (Figure 3b,c) was utilized to assess the metal dissolution induced by the acidic electrolyte and applied oxidative potentials. Using this stability protocol with alternating CAs and CVs, Mn-based oxychlorides show enhanced OER performance and reduced Mn dissolution compared to their oxide counterpart, γ-MnO_2, suggesting that the incorporation of Cl into the materials promotes the OER and stabilizes surface Mn when exposed to periods of constant and dynamic potential control. The $Mn_8O_{10}Cl_3$ activity remains stable for at least 2 h, followed by slight degradation

https://doi.org/10.1021/acs.chemmater.3c02362
Chem. Mater. 2024, 36, 1299−1307

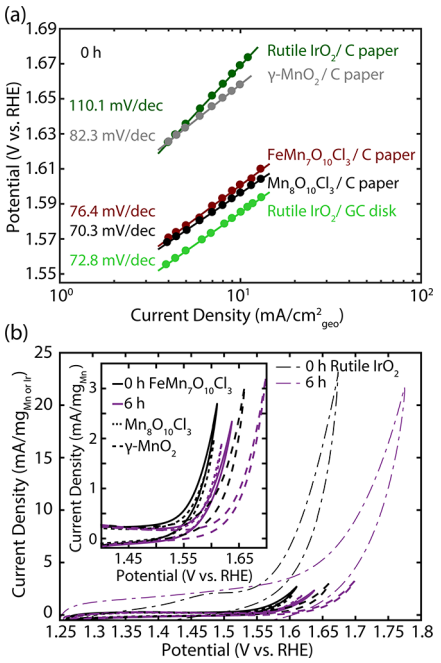

Figure 2. (a) Tafel plot of oxychlorides and oxides at 0 h derived from CV data. (b) Mass activities of oxychlorides and oxides/carbon paper electrodes at 0 h and after 6 h CA.

after 4 h. Overall, this catalyst reaches 10 mA/cm^2_{geo} with 367 mV of overpotential at 0−2 h and 384 mV at 6 h. Comparatively, the initial activity of $FeMn_7O_{10}Cl_3$ is nearly identical to that of $Mn_8O_{10}Cl_3$ but starts to decline slightly after only 0.25 h CA, finally requiring an overpotential of 405 mV to reach 10 mA/cm^2_{geo} after 6 h. Commercial rutile IrO_2 drop-cast on carbon paper is used as a benchmark to compare catalyst activity using the same electrode geometry and after stability testing conditions identical with those of the Mn-based catalysts. The Mn-based oxychloride catalysts exhibit superior OER performance compared to the rutile IrO_2 on carbon paper over the entire testing time (Figures 2, 3, and S3). We do note that rutile IrO_2 is reported to exhibit higher activity when deposited on glassy carbon substrates compared to carbon paper substrates,[27,28] as we also observe here.

When activity is normalized to the mass of Mn (or Ir), the activity trends for the Mn-based catalysts are similar to that of the area-normalized data, though the initial activity of the Fe-substituted material is slightly better (Figure 2b). As expected, the mass activity of rutile IrO_2 is superior to the Mn-based catalysts, by approximately 1 order of magnitude. Interestingly, the global production of Ir is about 6 orders of magnitude lower than Mn[29] due to lower crustal abundance, contributing to a significantly higher cost for Ir. Collectively, results for the oxychlorides indicate that selectively replacing Mn with Fe in the oxide octahedra may not significantly influence the catalytic activity but plays a crucial role in destabilizing the catalyst structure during the OER. The inferior stability of $FeMn_7O_{10}Cl_3$ can be partially attributed to a higher dissolution of Mn from the mixed Fe/Mn catalyst (average of 6.4 ± 0.3%) compared to $Mn_8O_{10}Cl_3$ (average of 5.1 ± 0.4%). This result somewhat contrasts the Pourbaix diagrams in Figure S4 that predict a slightly higher thermodynamic stability for $FeMn_7O_{10}Cl_3$ (0.73 eV/atom) versus $Mn_8O_{10}Cl_3$ (0.78 eV/atom). Our observation suggests that kinetic effects may be at play, specifically that $Mn_8O_{10}Cl_3$ may exhibit higher kinetic

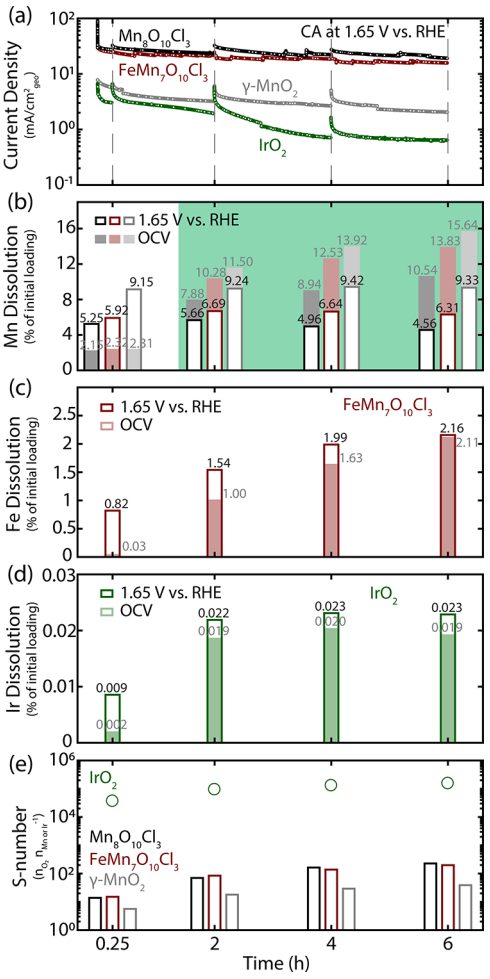

Figure 3. Stability of oxychlorides and oxides/carbon paper electrodes. (a) Current response during CA hold at 1.65 V vs RHE. Dissolution of (b) Mn and (c) Fe resulting from CV and CA hold at 1.65 V vs RHE (white bars with colored outlines) and from resting at OCV in identical electrolytes (shaded bars). Green background shading indicates time points where the application of an oxidizing potential had a stabilization effect and reduced the metal dissolution. Black: $Mn_8O_{10}Cl_3$, maroon: $FeMn_7O_{10}Cl_3$, gray: γ-MnO_2. (d) Ir dissolution. (e) Transient S-number calculated based on the faradaic charge passed and the amount of dissolved Mn or Ir at each individual time point.

stability[30] or that the restructured surface of $Mn_8O_{10}Cl_3$ formed under reaction conditions may exhibit a higher kinetic stability.[31] While a greater fraction of Mn dissolves from the material compared to Fe, it is likely that the dissolution of both elements from $FeMn_7O_{10}Cl_3$ also contributes to the greater Mn dissolution compared to $Mn_8O_{10}Cl_3$. Surprisingly, the partial replacement of Mn with the more electronegative Fe in the oxychloride decreases both the catalytic performance and material stability (increased dissolution), suggesting new material dynamics and catalyst behavior for HAMs that differ from that of previous computational study on Mn-based oxides.[23]

A second stability protocol utilizing only CA holds at 1.65 V versus RHE (without intermittent CVs) was also employed to distinguish the impact of constant versus dynamic applied oxidative potentials. Comparing the outcomes of these stability protocols (with and without CV), we note that the electrochemical performance of the oxychlorides is nearly

https://doi.org/10.1021/acs.chemmater.3c02362
Chem. Mater. 2024, 36, 1299−1307

identical under both protocols, but there is a slightly increased (1−2.5×) dissolution when periods of variable potential control (CVs) are included in the stability test (Figure S5). In contrast, γ-MnO_2 demonstrates a significant decrease in OER current in parallel with 3× increase in Mn dissolution for the protocol including CV curves, suggesting that periods of variable potential control introduce additional material dynamics in γ-MnO_2 which decrease both material and performance stabilities. This suggests that the incorporation of chlorine to synthesize $Mn_8O_{10}Cl_3$ results in a catalyst material that is more resistant to dissolution and activity decline under dynamic potential conditions, resulting in a material that may be more resistant to degradation under startup/shutdown cycles or other examples of variable operation. Referring again to the Pourbaix diagrams, (Figure S4) there are a range of different species that are expected to be the most stable under the range of potentials sampled during CV. It is likely that Mn enters an unstable OER regime during CV, where it may undergo Mn^{2+} dissolution below 1.4 V and Mn^{2+}/Mn^{3+} transition above 1.4 V in acid,[34,35] contributing to higher Mn dissolution, compared to operation at a constant applied potential of 1.65 V versus RHE.

Contributions of Electrolyte and Potential to Metal Dissolution. While catalyst material and performance stability are not always directly linked, metal dissolution can affect the OER performance by altering the reactivity and stability of the remaining, restructured catalyst surface. In particular, the influence of acidic electrolytes and oxidizing potentials on metal dissolution from HAMs during long-term operation is not yet understood. To address this question, we compare the catalyst dissolution behavior upon exposure to these electrochemical stability-testing protocols (featuring CAs at 1.65 V versus RHE) with the dissolution behavior of catalysts left at the open-circuit voltage (OCV) in the same electrolyte (Figures 3b,c and S5c,d). Electrolyte aliquots sampled during electrochemical testing that includes CV and constant potential holds at 1.65 V versus RHE reveal that Mn dissolution ranges from 4.6 to 9.4% of the initial Mn loading for this set of catalysts, with the highest Mn loss observed for γ-MnO_2 and the least Mn loss observed for $Mn_8O_{10}Cl_3$. For stability testing that only includes constant potential holds, Mn dissolution is lower overall, ranging from 2.1 to 5.9% of the initial Mn loading, where $Mn_8O_{10}Cl_3$ and γ-MnO_2 experience similar dissolution and the highest Mn loss is now observed for $FeMn_7O_{10}Cl_3$. In either case, all catalysts exhibit higher rates of Mn dissolution during the first 0.25 h, followed by a period of relative stability where only an additional 0−2% of initial Mn loading is dissolved over the next 6 h, indicating that the reconstructed surface formed under reaction conditions helps stabilize Mn. Previous studies have discovered that the dissolved Mn^{2+} species can redeposit onto the working electrode as γ-MnO_2,[34] and Mn^{3+} species can undergo disproportionation to form Mn^{2+} and Mn^{4+} between 1.6 and 1.75 V versus RHE.[34,35] Given the observed minor decrease in the dissolved Mn content over time for some of these samples, we propose that this may be caused by a balance between some amount of Mn dissolution and redeposition along with structural changes in the material.

In contrast, purely chemical dissolution induced by exposure to the acidic electrolyte at the OCV reveals a different trend (Figure 3b,c). While initial Mn dissolution (0.25 h) in acidic electrolyte is somewhat reduced at the OCV compared to that at 1.65 V versus RHE, Mn dissolution increases significantly with increased exposure time at the OCV, following the order of γ-MnO_2 > $FeMn_7O_{10}Cl_3$ > $Mn_8O_{10}Cl_3$. First, this result indicates that incorporation of Cl helps mitigate chemical dissolution of Mn under stability testing that includes dynamic potential control; however, partial substitution of Fe in the structure reintroduces chemical instability in acid regardless of electrochemical testing protocol. Second, this result highlights the protective impact of an oxidizing potential for Mn. It is likely that fast material dynamics upon the first exposure to acid are exacerbated by an oxidizing potential, leading to greater Mn leaching during initial OER testing (0.25 h). However, interestingly, the application of an oxidative potential mitigates further Mn leaching for the remainder of testing time; Mn dissolution is decreased by ∼4−12% over this time period, for application of dynamic or constant oxidative potentials. Together, these results suggest that surface Mn species supported by high oxidizing potential have slower dissolution kinetics and tend to transform into more stable Mn species.

In contrast to Mn dissolution, Fe dissolution (Figures 3c and S5d) from $FeMn_7O_{10}Cl_3$ in acid is exacerbated by the application of an oxidative potential at all time points, as is more commonly observed for many transition-metal oxides. The initial Fe dissolution under 1.65 V versus RHE is much greater than that at OCV; the electrode under oxidative potential loses nearly 0.8% of its total Fe loading to the electrolyte in the first 0.25 h. This initial loss of material carries through the remainder of the observation period, where a similar stability is observed, and little additional Fe is lost from the electrode under either condition for 0.25−6 h. The small amount of Fe dissolved overall (∼2−4% of total Fe loading for both stability protocols) may be attributed to the bonding environments of [FeO_6] embedded into the structure, which makes Fe less prone to dissolving under harsh conditions.

We further analyzed the dissolution data to calculate the respective S-numbers for the Mn-based catalysts and our benchmark IrO_2. S-number is defined as the ratio between the amount of evolved oxygen (based on faradaic charge passed) and the amount of dissolved metal and has been used as a metric to assess the stability of precious metal catalysts.[32] This metric is usually calculated based on the data collected after the system has reached a steady state, which ignores early-stage dissolution behavior.[33] Here, the "transient" S-number (Figure 3e) is calculated based on the change in faradaic charge and the amount of dissolved Mn or Ir at each individual time point such that it reflects the dynamic behavior of the catalyst material as a function of stability testing time. For the stability testing protocol, which utilizes alternating CA holds and CVs, the Mn-based oxychlorides demonstrate higher stability compared to the surfaces formed on γ-MnO_2. Still, Mn exhibits a much greater dissolution in all these materials compared to Ir, resulting in S-numbers for Mn between 40 and 200 (after 6 h CA, Table S4), which is 2 orders of magnitude lower than that of Ir in rutile IrO_2 (1.5×10^5 after 6 h CA). For all materials, the transient S-number increases after the first 0.25 h CA at 1.65 V versus RHE, indicating a transformation to more active and stable catalyst phases. The similar Mn (or Ir) dissolution and transient S-number during degradation (4 and 6 h) indicate the eventual stabilization of the reconstructed catalyst phases.

Surface Chemical and Near-Surface Bulk Electronic Properties. *Ex situ* X-ray photoelectron spectroscopy (XPS) and XAS were carried out to understand the catalyst material

https://doi.org/10.1021/acs.chemmater.3c02362
Chem. Mater. 2024, 36, 1299−1307

dynamics upon the OER and to correlate these changes in surface chemical and near-surface bulk electronic properties with the activity performance. The XPS peak positions of $FeMn_7O_{10}Cl_3$ observed at 724.5 eV for Fe $2p_{1/2}$ and 711.0 eV for Fe $2p_{3/2}$ correspond to Fe^{3+} in α-Fe_2O_3 (Figure 4a).[36]

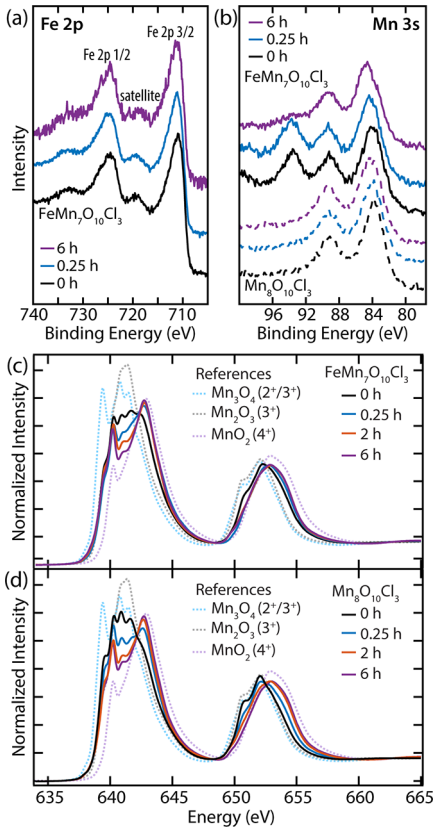

Figure 4. Surface and near-surface bulk metal valence. *Ex situ* (a) Fe 2p and (b) Mn 3s XPS spectra of Mn-based oxychlorides in pristine state and after 0.25 h CA and 6 h CA. $FeMn_7O_{10}Cl_3$ is shown in solid lines, and $Mn_8O_{10}Cl_3$ is shown in dashed lines. The additional peak located at ~93 eV in Mn 3s for $FeMn_7O_{10}Cl_3$ is due to the excitation of the neighboring Fe 3s. Mn $L_{III,II}$-edge spectra of pristine and electrochemically tested samples of (c) $FeMn_7O_{10}Cl_3$ and (d) $Mn_8O_{10}Cl_3$.

Additionally, the presence of an Fe $2p_{3/2}$ satellite peak at 718.9 eV further confirms that the surface of $FeMn_7O_{10}Cl_3$ primarily consists of Fe^{3+} species (this satellite peak is positioned ~4 eV lower in energy for the Fe^{2+} species). These features are considerably noisier after 6 h of testing due to Fe leaching from the surface, as previously discussed in the ICP-MS analysis. XPS also reveals Mn^{3+} surface species in the pristine forms of both $FeMn_7O_{10}Cl_3$ and $Mn_8O_{10}Cl_3$ based on the splitting of the Mn 3s core-level peaks (Figures 4b, S8 and Table S5). Upon OER testing, surface Mn is oxidized to a near 4+ state, reflecting a change in chemical species at the surface under oxidizing and acidic conditions.

To further characterize the near-surface bulk Mn valence before and after short-term and long-term stability testing, we performed *ex situ* total electron yield (TEY) Mn L-edge soft XAS measuring both the L_{III} and L_{II} regions (Mn $2p_{3/2}$ and Mn $2p_{1/2}$, respectively, Figure 4c,d). The XAS spectra of both pristine oxychloride materials closely match those of Mn_3O_4 and Mn_2O_3 (Figure S10), displaying the characteristic peaks between 640 and 642, as well as a shoulder at ~650 eV. The additional presence of a small shoulder prior to 640 eV, which is unique to Mn_2O_3, suggests the existence of a 3+ oxidation state. The distinct spectral shapes of the pristine oxychlorides with and without Fe incorporation (Figure S11a) indicate a difference in the material electronic structure, likely due to the substitution of the more electronegative Fe in octahedral sites. After electrochemical testing, the near-surface bulk Mn in all tested samples is oxidized to a 4+ state; this is evident from the increasing peak intensity at ~643 eV in the L_{III} region and the shift toward higher energy (~653 eV) in the L_{II} region. After 0.25 h CA hold at 1.65 V versus RHE, $FeMn_7O_{10}Cl_3$ undergoes significant oxidation to Mn^{4+}, while $Mn_8O_{10}Cl_3$ undergoes a slower change and is only slightly oxidized from its pristine state, primarily resembling a mixed $Mn^{2+/3+}$ oxidation state. With prolonged testing, both materials exhibit an increased Mn^{4+} character, as shown by the deeper "valley" between the two distinct transitions in the L_{III} region, consistent with XPS results.[37] Furthermore, the similar spectra obtained after 2 h CA (and 6 h CA, Figure S11b) suggest that the reconstructed surfaces of both materials may have a similar electronic structure. Considering these results along with the catalytic activity and Mn dissolution results, we find that the formation of Mn^{4+} on the catalyst surface stabilizes surface Mn atoms and prevents aggressive leaching but mildly impedes OER kinetics as these materials experience a slight increase in overpotential in parallel with the increased oxidation state and reduced Mn leaching.

Dynamics of Bulk Fe and Mn in Oxychlorides during OER. The bulk properties of pristine materials and *in situ* material dynamics were also analyzed using a hard X-ray absorption near-edge structure (XANES) and extended X-ray absorption fine structure (EXAFS). *Ex situ* XANES measurements at the Fe K-edge (Figure S12a,b) were conducted to track changes in the average, bulk Fe oxidation state after exposing samples to various electrochemical conditions. The consistent pre-edge peaks at ~7114.5 eV and edge positions at ~7123.2 eV for samples before and after OER are close to Fe^{3+} [38,39] and consistent with the expected Fe valence in the form of $[FeO_6]$ in oxychloride. Complementary *in situ* XANES at Fe K-edge (Figure S12c) was also used to monitor the evolution of bulk Fe valency in real time during OER testing; these spectra do not display a decrease in signal or significant changes in the edge position or pre-edge feature over the course of CA testing time, indicating a constant Fe valence. Overall, both measurements show that $FeMn_7O_{10}Cl_3$ consists of Fe^{3+} species, and bulk Fe remains stable during electrochemical testing regardless of surface Fe leaching.

XANES and EXAFS measurements reveal a more dynamic story for these oxychloride catalysts when measured at the Mn K-edge. Due to the complexity in the origin of pre-edge features in the Mn K-edge XANES spectra (discussed in the Supporting Information), we primarily focus on the Mn K-edge position to evaluate the bulk Mn oxidation state of pristine and OER-tested oxychlorides. As shown in the *ex situ* Mn K-edge XANES in Figure 5a, both pristine oxychloride catalysts exhibit a Mn valence between 2+ and 3+ states. *In situ* XANES reveals nearly identical spectra when measured at various potentials (anodically and cathodically stepped CA holds from the OCV to 1.65 V versus RHE, Figure S14a–c), as well as when held at 1.65 V versus RHE for up to 6 h (Figure S14d–f). Comparing these results with those obtained from soft XAS and XPS, we find that the bulk manganese exists in a mixture of 2+/3+ states, while the (near-)surface exhibits

https://doi.org/10.1021/acs.chemmater.3c02362
Chem. Mater. 2024, 36, 1299−1307

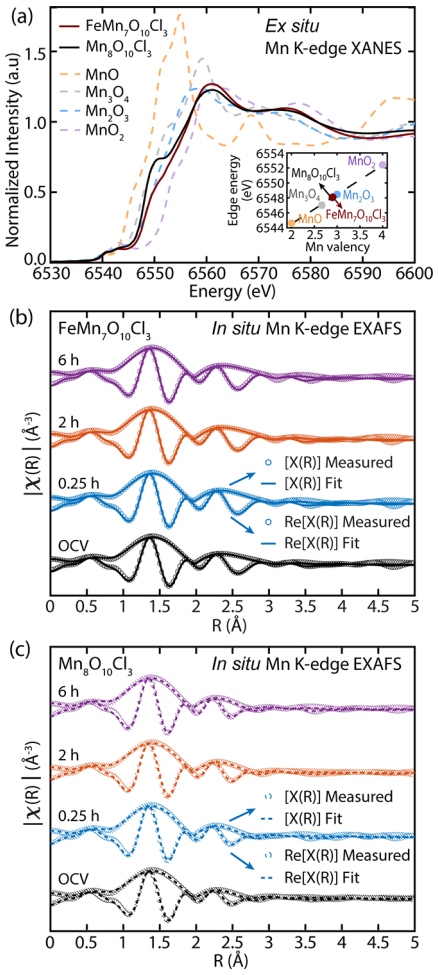

Figure 5. Bulk electronic and geometric structures. (a) *Ex situ* Mn K-edge XANES spectra of pristine oxychlorides and standards (manganosite MnO, hausmannite Mn_3O_4, bixbyite Mn_2O_3, and pyrolusite MnO_2). Inset shows the trend line for edge energy and Mn valency generated by standards (y = 3.9165x + 6536.7, R^2 = 0.9998). *In situ* Mn K-edge EXAFS measurements and fits of (b) $FeMn_7O_{10}Cl_3$ and (b) $Mn_8O_{10}Cl_3$ at OCV and at 1.65 V vs RHE after 0.25 2, and 6 h.

primarily Mn^{3+} for the pristine materials and then transforms to a Mn^{4+}-rich surface phase after OER testing at 1.65 V versus RHE.

Fitting of EXAFS measured *in situ* at the Mn K-edge provides insights into the bonding environments in oxychlorides as a function of applied potential and time. As the potential is increased from the OCV to 1.65 V versus RHE, $FeMn_7O_{10}Cl_3$ shows a reduction in the Mn−Cl bond length within the chloride octahedra, while the geometric structure of $Mn_8O_{10}Cl_3$ remains unchanged (Figure S16 and Table S7). We therefore correlate the reduced Mn−Cl bond length in $FeMn_7O_{10}Cl_3$ with a significant increase in Mn^{4+} species, while we attribute a stable [$MnCl_6$] configuration with Mn maintained in a 2+/3+ state, at least over these short timescales. Furthermore, reducing the potential back to the OCV results in a re-expansion of the Mn−Cl bond in $FeMn_7O_{10}Cl_3$, indicating a dynamic, reversible response to the applied potential. We also measured *in situ* EXAFS while the samples were held at 1.65 V versus RHE for up to 6 h (Figure 5b,c). Over this time period, both materials exhibit stable oxychloride octahedra throughout testing but show different trends in the change of chloride octahedra (Table S7). Specifically, the Mn−Cl bond length of [$MnCl_6$] within $Mn_8O_{10}Cl_3$ elongates after 2 h of CA (∼0.02 Å) and then contracts after 6 h of CA (∼0.05 Å), correlating with the electrode activation and degradation, respectively. In contrast, $FeMn_7O_{10}Cl_3$ experiences a continuous decrease in the Mn−Cl bond length during the first 2 h of testing, after which the structure is maintained, accompanied by a continuous decrease in the OER performance. Together, the dynamic bond length of Mn−Cl during the activation and degradation processes suggests a compromise between increasing Mn valence and maintaining structural integrity.

CONCLUSIONS

In summary, we employ oxychloride materials that utilize earth-abundant metals to systematically tune catalyst properties and probe dynamic material responses to well-controlled reaction conditions. Mn-based oxychlorides exhibit enhanced OER performance compared with their oxide counterparts, and the selective substitution of Fe^{3+} in the oxide octahedra of $Mn_8O_{10}Cl_3$ maintains catalytic activity upon exposure to acid but destabilizes the oxychloride materials, inducing greater metal dissolution and faster oxidation of surface Mn species under the same reaction conditions. This indicates that the chloride or oxychloride units likely contribute more to enhanced activity, while the oxide units ([MO_6], where M = Mn or Fe) play a more significant role in the catalytic stability. Operating at a high potential (1.65 V versus RHE) mitigates manganese leaching from all materials during prolonged exposure to OER conditions, resulting in improved atomic stability compared to the exposure to identical pH electrolyte at OCV.

Progressively probing the surface, near-surface, and bulk electronic structure with XPS plus soft and hard XAS, we find an overall agreement that the initial $Mn^{2+/3+}$ states consistently oxidize toward a more stabilized Mn^{4+} at the surface with increased testing time, although this change occurs more quickly for the Fe-substituted material. Parallel monitoring of the geometric structures over extended time periods reveals that the partial substitution of Fe induces a reversible reduction in Mn−Cl bond lengths within the chloride octahedra of $FeMn_7O_{10}Cl_3$ as a function of applied potential, while $Mn_8O_{10}Cl_3$ exhibits an elongation and contraction of Mn−Cl bonds at short and long testing times, respectively. These results suggest that the formation of active sites with primarily Mn^{3+} states and elongated Mn−Cl bonds promotes OER, while an increase in Mn^{4+} sites and compressed [$MnCl_6$] octahedra impedes the reaction kinetics. These results reflect the importance of considering the impact of reaction conditions on material transformations as well as the impacts of complementary cation and anion engineering to modify the electronic and geometric structures of transition-metal active sites to support the enhanced activity and stability for acidic water oxidation.

METHODS

Materials Synthesis. For Mn-based oxychlorides, stoichiometric mixtures of $Mn(NO_3)_2{\cdot}4H_2O$ (98%, Thermo Scientific, dissolved in isopropanol) and $MnCl_2{\cdot}4H_2O$ (≥98%, Sigma-Aldrich) or $FeCl_3{\cdot}6H_2O$ (99+%, Thermo Scientific, dissolved in H_2O) were mixed, and 48 μL of the resulting solution was drop-cast on 1 × 1 cm^2 carbon paper (Sigracet 39 AA, Fuel Cell Store) before heating at 250 °C for 5 h. After cooling to room temperature, the as-prepared carbon paper

https://doi.org/10.1021/acs.chemmater.3c02362
Chem. Mater. 2024, 36, 1299−1307

was sonicated in H_2O for 30 s before use. γ-MnO_2 was prepared by using a similar method without the addition of chloride precursor. The mass loadings of Mn are ~6.6, 4.9, and 3.5 mg/cm^2 for $Mn_8O_{10}Cl_3$, $FeMn_7O_{10}Cl_3$, and γ-MnO_2, respectively. For Ir reference, commercial rutile IrO_2 (Sigma-Aldrich, 99.9% trace metal basis) powder was dispersed in a liquid solution composed of 97% v/v isopropyl alcohol (Fisher Chemical) and 3% v/v Nafion 117 (Sigma-Aldrich, 5% in a mixture of lower aliphatic alcohols and water) with a Vulcan carbon support (XC-72, FuelCellStore, 1:1 mass ratio to catalyst). The ink was drop-cast onto either a carbon paper (1 cm^2) or an inert glassy carbon disk (0.196 cm^2) to achieve a mass loading of 0.48 mg Ir/cm$^2_{geo}$.

Electrochemical Testing. The electrochemical measurement was conducted in a single compartment with 40 mL of 0.1 M $HClO_4$ (Alfa Aesar, pH 1.14) using a three-electrode setup, with Ag/AgCl (4 M KCl) as the reference electrode, Pt wire as the counter electrode, and an oxychloride (or oxide)/carbon paper electrode as the working electrode. The Ag/AgCl reference electrode was calibrated to the reversible hydrogen electrode (RHE) in the identical electrolyte prior to electrochemical measurements. The solution was purged with N_2 to remove O_2 before testing.

Electrical impedance spectroscopy (EIS) was conducted at an open-circuit voltage (OCV) in a frequency range between 500 kHz and 1 mHz prior to electrochemical testing to determine the solution resistance. For Mn-based materials, the catalyst activity was measured by conducting two CV test scanning between 0.97 and 1.5 V versus Ag/AgCl at a rate of 1 mV/s. For Ir-based materials, five CV scans were measured at 20 mV/s, and the third CV was used for data analysis. Extensive chronoamperometry (CA) test was conducted at 1.65 V versus RHE for 6 h. In order to maintain the potential during CA, the potential is compensated with 85% by ZIR.

Materials Characterization. The crystal structures of the pristine samples were monitored by X-ray diffraction (XRD) at a shallow angle (0.6°, to enhance the signal from the sample compared to the substrate; Cu Kα radiation, Smartlab). X-ray photoelectron spectroscopy (XPS) was conducted with a Thermo Scientific ESCALAB 250Xi (0.5 eV) instrument with a monochromatic Al Kα source and 500 μm spot size. All XPS fitting was completed using CasaXPS software, and all spectra were calibrated to the adventitious carbon C 1s peak at 284.8 eV. The material morphology was confirmed by scanning electron microscopy (SEM) performed on a Hitachi SU8030 system. Aliquots of the electrolyte were taken after 0.25, 2, 4, and 6 h of activity testing via CAs to measure the electrochemical metal dissolutions at each corresponding time point. Comparative tests to acquire the chemical metal dissolutions due to the electrolyte alone were conducted in the same setup without applying any potential. *Ex situ* soft X-ray absorption spectroscopy (XAS) on the Mn L-edge was performed on beamline 8−2 at SSRL using a 1100 lines/mm spherical grating monochromator using 40 × 40 μm slits, providing ~10^{10} photons/s at 0.35 eV resolution in a 0.5 mm^2 beam spot in the 600−650 eV range. Total electron yield data (TEY) were acquired in a single load at room temperature and under an ultrahigh vacuum (10^{-9} Torr). All spectra were normalized by the incoming flux, measured from a thin grid with freshly evaporated gold positioned upstream of the sample chamber. A few percents of the beam were also intercepted upstream by an MnO reference sample which was measured simultaneously and used to calibrate the energy of all scans with a relative energy precision of ±25 meV. Reference powders were purchased (Mn_3O_4, 97%, Strem Chemicals; Mn_2O_3, 99.999%, Sigma-Aldrich; and MnO_2, 97%, Thermo Scientific) and used as received, mounted on an aluminum sample stick using a conductive carbon tape. Data were processed such that a baseline was subtracted, and the area was normalized within the range of 636 to 660 eV. *Ex situ* hard XAS on the Mn and Fe K-edge were completed at Sector 5.BMD of the X-ray Science Division beamlines at the Advanced Photon Source, Argonne National Laboratory. Photon energy was calibrated by applying the appropriate offset to shift the simultaneously measured reference spectra of Mn foil to 6539 eV and Fe foil to 7112 eV, respectively. *Ex situ* X-ray absorption near-edge structure (XANES) and extended X-ray absorption fine structure (EXAFS) spectra of all samples were acquired in transmission mode. *In situ* XAS electrochemical cells were back-illumination-type cells. The carbon papers were secured to fit an opening (1 × 1 cm^2) in the wall of the container with a Kapton tape (Figure S1). Electrical contact to the working electrode carbon paper was made via contact with the copper tape. A Pt wire counter electrode and an Ag/AgCl reference electrode were used, as is consistent with the other electrochemical testing reported throughout this work.

For $FeMn_7O_{10}Cl_3$, Mn spectra were collected in fluorescence mode after holding the potential at OCV (~1.2 V versus RHE), 1.36, 1.46, 1.55, 1.60, 1.65 V versus RHE (and reverse) for 15 min each in 0.1 M $HClO_4$, followed by a final potential hold at 1.65 V versus RHE for 6 h during which both Mn spectra (XANES and first-shell EXAFS) and Fe spectra (XANES) were collected after 2 and 6 h of the final CA hold. For $Mn_8O_{10}Cl_3$, Mn spectra were collected in fluorescence mode using a silicon drift detector after holding the potential at the OCV (~1.2 V versus RHE) for 15 min and 1.65 V versus RHE for 6 h during which spectra were collected after 0.25, 2, and 6 h of CA. XAS data were processed using Athena (https://bruceravel.github.io/demeter/documents/Athena/index.html), and Artemis (https://bruceravel.github.io/demeter/documents/Artemis/index.html) software.

Quantification of Mn and Fe was accomplished using inductively coupled plasma-mass spectrometry (ICP-MS) of acidified samples by using the following procedure: for each sample, 1 mL of sample was passed through a 0.45 μm syringe filter directly into a 15 mL metal-free centrifuge tube. The collected filtrate (~700 μL) was acidified with 300 μL concentrated trace nitric acid (HNO_3, >69%, Thermo Fisher Scientific, Waltham, MA, USA) and heated for 3 h in a 65 °C water bath. The final sample was diluted with 5 mL of ultrapure H_2O (18.2 MΩ cm) to produce a 6 mL sample volume in a matrix of 5% HNO_3 (v/v). A quantitative standard was made using a mixed elemental standard containing 100 μg/mL each of Mn and Fe (Inorganic Ventures, Christiansburg, VA, USA). This was diluted with 5% HNO_3 (v/v) to create a calibration standard containing 1000 ng/g Mn and Fe in a total sample volume of 50 mL. A solution of 5% (v/v) HNO_3 was used as the calibration blank. ICP-MS was performed on a computer-controlled (QTEGRA software) Thermo iCapQ ICP-MS system (Thermo Fisher Scientific, Waltham, MA, USA) operated in KED mode and equipped with an ESI SC-2DX PrepFAST autosampler (Omaha, NE, USA). Internal standard was added inline using the prepFAST system and consisted of 1 ng/mL of a mixed element solution containing Bi, In, Li, Sc, Tb, and Y (IV-ICPMS-71D from Inorganic Ventures). Online dilution was also carried out by the prepFAST system and used to generate a calibration curve consisting of 1000, 500, 200, 100, 50, 20, 10, 5, and 1 ppb Mn and Fe. Each sample was acquired using one survey run (10 sweeps) and three main (peak jumping) runs (40 sweeps). The isotopes selected for analysis were ^{55}Mn, ^{56,57}Fe, ^{45}Sc, and ^{89}Y (chosen as internal standards for data interpolation and machine stability).

■ ASSOCIATED CONTENT

Supporting Information

The Supporting Information is available free of charge at https://pubs.acs.org/doi/10.1021/acs.chemmater.3c02362.

In situ XAS setup; SEM figures of Mn-based catalysts before and after OER; geometric and mass activities of Mn-based catalysts and benchmark Ir material; Pourbaix diagrams of Mn-based oxychlorides; stability of Mn-based catalysts under different stability testing protocols; activity and stability of commercial rutile IrO_2; *ex situ* Fe 2p, Mn 3s, and Cl 2p XPS spectra; *ex situ* Mn L-edge XAS data; *ex situ* and *in situ* Fe and Mn K-edge XANES data; and *in situ* Mn K-edge EXAFS data/fitting details (PDF).

https://doi.org/10.1021/acs.chemmater.3c02362
Chem. Mater. 2024, 36, 1299−1307

AUTHOR INFORMATION

Corresponding Author

Linsey C. Seitz − *Department of Chemical and Biological Engineering, Northwestern University, Evanston, Illinois 60208-3113, United States;* orcid.org/0000-0001-6831-6747; Email: linsey.seitz@northwestern.edu

Authors

Ruihan Li − *Department of Chemical and Biological Engineering, Northwestern University, Evanston, Illinois 60208-3113, United States;* orcid.org/0000-0001-5193-8523

Dennis Nordlund − *SLAC National Accelerator Laboratory, Menlo Park, California 94025, United States*

Complete contact information is available at: https://pubs.acs.org/10.1021/acs.chemmater.3c02362

Author Contributions

R.L. contributed to the conceptualization, data curation, formal analysis, investigation, methodology, and writing of the original draft of this work. D.N. contributed to the data curation of *ex situ* soft XAS experiment, review, and editing of this work. L.S. contributed to the conceptualization, methodology, resources, supervision, review, and editing of this work. The manuscript was written through contributions of all authors. All authors have given approval to the final version of the manuscript.

Funding

This work was supported by a National Science Foundation CAREER Award (2144365-CBET).

Notes

The authors declare no competing financial interest.

ACKNOWLEDGMENTS

This work made use of the Jerome B. Cohen X-ray Diffraction Facility supported by the MRSEC program of the National Science Foundation (DMR-2308691) at the Materials Research Center of Northwestern University and the Soft and Hybrid Nanotechnology Experimental (SHyNE) Resource (NSF ECCS-1542205). Metal analysis was performed at the Northwestern University Quantitative Bioelement Imaging Center (QBIC) generously supported by the NIH under grant S10OD020118. This work made use of the EPIC and Keck-II facilities of Northwestern University's NUANCE Center, which have received support from the SHyNE Resource (NSF ECCS-2025633), the IIN, and Northwestern's MRSEC program (NSF DMR-1720139). Hard XAS measurement was performed at the DuPont-Northwestern-Dow Collaborative Access Team (DND-CAT) located at Sector 5 of the Advanced Photon Source (APS). DND-CAT is supported by Northwestern University, The Dow Chemical Company, and DuPont de Nemours, Inc. This research used resources of the Advanced Photon Source, a U.S. Department of Energy (DOE) Office of Science User Facility operated for the DOE Office of Science by Argonne National Laboratory under Contract No. DE-AC02-06CH11357. The authors graciously acknowledge the help of Denis Keane and Qing Ma for their assistance with XAS experimentation at the 5-BM-D Advanced Photon Source. Use of the Stanford Synchrotron Radiation Lightsource, SLAC National Accelerator Laboratory, is supported by the U.S. Department of Energy, Office of Science, Office of Basic Energy Sciences under Contract No. DE-AC02-76SF00515. The authors graciously acknowledge the assistance of Rebecca Sponenburg with metal analysis at QBIC. The authors also graciously acknowledge Adrien Deberghes for his help with designing the *in situ* XAS cell.

REFERENCES

(1) Man, I. C.; Su, H. Y.; Calle-Vallejo, F.; Hansen, H. A.; Martinez, J. I.; Inoglu, N. G.; Kitchin, J.; Jaramillo, T. F.; Norskov, J. K.; Rossmeisl, J. Universality in Oxygen Evolution Electrocatalysis on Oxide Surfaces. *ChemCatChem.* **2011**, *3* (7), 1159−1165.

(2) Danilovic, N.; Subbaraman, R.; Chang, K. C.; Chang, S. H.; Kang, Y. J. J.; Snyder, J.; Paulikas, A. P.; Strmcnik, D.; Kim, Y. T.; Myers, D.; Stamenkovic, V. R.; Markovic, N. M. Activity-Stability Trends for the Oxygen Evolution Reaction on Monometallic Oxides in Acidic Environments. *J. Phys. Chem. Lett.* **2014**, *5* (14), 2474−2478.

(3) McCrory, C. C.; Jung, S.; Ferrer, I. M.; Chatman, S. M.; Peters, J. C.; Jaramillo, T. F. Benchmarking hydrogen evolving reaction and oxygen evolving reaction electrocatalysts for solar water splitting devices. *J. Am. Chem. Soc.* **2015**, *137* (13), 4347−57.

(4) Suntivich, J.; May, K. J.; Gasteiger, H. A.; Goodenough, J. B.; Shao-Horn, Y. A Perovskite Oxide Optimized for Oxygen Evolution Catalysis from Molecular Orbital Principles. *Science* **2011**, *334* (6061), 1383−1385.

(5) Seitz, L. C.; Dickens, C. F.; Nishio, K.; Hikita, Y.; Montoya, J.; Doyle, A.; Kirk, C.; Vojvodic, A.; Hwang, H. Y.; Norskov, J. K.; Jaramillo, T. F. A highly active and stable IrOx/SrIrO3 catalyst for the oxygen evolution reaction. *Science* **2016**, *353* (6303), 1011−1014.

(6) Harada, J. K.; Charles, N.; Poeppelmeier, K. R.; Rondinelli, J. M. Heteroanionic Materials by Design: Progress Toward Targeted Properties. *Adv. Mater.* **2019**, *31* (19), No. e1805295.

(7) Lemoine, K.; Lhoste, J.; Hemon-Ribaud, A.; Heidary, N.; Maisonneuve, V.; Guiet, A.; Kornienko, N. Investigation of mixed-metal (oxy)fluorides as a new class of water oxidation electrocatalysts. *Chem. Sci.* **2019**, *10* (40), 9209−9218.

(8) Ghanem, M. A.; Amer, M. S.; Al-Mayouf, A. M.; Arunachalam, P.; Weller, M. T. Halide-Doping Effect of Strontium Cobalt Oxide Electrocatalyst and the Induced Activity for Oxygen Evolution in an Alkaline Solution. *Catalysts* **2021**, *11* (11), 1408.

(9) Miyahara, Y.; Miyazaki, K.; Fukutsuka, T.; Abe, T. Strontium cobalt oxychlorides: enhanced electrocatalysts for oxygen reduction and evolution reactions. *Chem. Commun.* **2017**, *53* (18), 2713−2716.

(10) El-Emam, R. S.; Zamfirescu, C.; Gabriel, K. S., Chapter 19 - Hydrogen production pathways for Generation-IV reactors. In *Handbook of Generation IV Nuclear Reactors*, (Second ed.), Pioro, I. L., Ed.; Woodhead Publishing: 2023; 665−680.

(11) Shiva Kumar, S.; Himabindu, V. Hydrogen production by PEM water electrolysis − A review. *Materials Science for Energy Technologies* **2019**, *2* (3), 442−454.

(12) Millet, P., 9 - Hydrogen production by polymer electrolyte membrane water electrolysis. In *Compendium of Hydrogen Energy*, Subramani, V.; Basile, A.; Veziroğlu, T. N., Eds.; Woodhead Publishing: Oxford, 2015; 255−286.

(13) Song, C. W.; Lim, J.; Bae, H. B.; Chung, S.-Y. Discovery of crystal structure−stability correlation in iridates for oxygen evolution electrocatalysis in acid. *Energy Environ. Sci.* **2020**, *13* (11), 4178−4188.

(14) Lee, Y.; Suntivich, J.; May, K. J.; Perry, E. E.; Shao-Horn, Y. Synthesis and Activities of Rutile IrO2 and RuO2 Nanoparticles for Oxygen Evolution in Acid and Alkaline Solutions. *J. Phys. Chem. Lett.* **2012**, *3* (3), 399−404.

(15) Ma, Z.; Zhang, Y.; Liu, S.; Xu, W.; Wu, L.; Hsieh, Y.-C.; Liu, P.; Zhu, Y.; Sasaki, K.; Renner, J. N.; Ayers, K. E.; Adzic, R. R.; Wang, J. X. Reaction mechanism for oxygen evolution on RuO2, IrO2, and RuO2@IrO2 core-shell nanocatalysts. *J. Electroanal. Chem.* **2018**, *819*, 296−305.

(16) Kim, J.; Shih, P. C.; Tsao, K. C.; Pan, Y. T.; Yin, X.; Sun, C. J.; Yang, H. High-Performance Pyrochlore-Type Yttrium Ruthenate

Electrocatalyst for Oxygen Evolution Reaction in Acidic Media. *J. Am. Chem. Soc.* **2017**, *139* (34), 12076−12083.
(17) Cao, L. L.; Luo, Q. Q.; Chen, J. J.; Wang, L.; Lin, Y.; Wang, H. J.; Liu, X. K.; Shen, X. Y.; Zhang, W.; Liu, W.; Qi, Z. M.; Jiang, Z.; Yang, J. L.; Yao, T. Dynamic oxygen adsorption on single-atomic Ruthenium catalyst with high performance for acidic oxygen evolution reaction. *Nat. Commun.* **2019**, *10*, 4849.
(18) Hao, S. Y.; Liu, M.; Pan, J. J.; Liu, X. N.; Tan, X. L.; Xu, N.; He, Y.; Lei, L. C.; Zhang, X. W. Dopants fixation of Ruthenium for boosting acidic oxygen evolution stability and activity. *Nat. Commun.* **2020**, *11* (1), 5368.
(19) Li, A.; Kong, S.; Guo, C.; Ooka, H.; Adachi, K.; Hashizume, D.; Jiang, Q.; Han, H.; Xiao, J.; Nakamura, R. Enhancing the stability of cobalt spinel oxide towards sustainable oxygen evolution in acid. *Nature Catalysis* **2022**, *5* (2), 109−118.
(20) Chong, L.; Gao, G.; Wen, J.; Li, H.; Xu, H.; Green, Z.; Sugar, J. D.; Kropf, A. J.; Xu, W.; Lin, X. M.; Xu, H.; Wang, L. W.; Liu, D. J. La- and Mn-doped cobalt spinel oxygen evolution catalyst for proton exchange membrane electrolysis. *Science* **2023**, *380* (6645), 609−616.
(21) Lemoine, K.; Gohari-Bajestani, Z.; Moury, R.; Terry, A.; Guiet, A.; Greneche, J. M.; Hemon-Ribaud, A.; Heidary, N.; Maisonneuve, V.; Kornienko, N.; Lhoste, J. Amorphous Iron-Manganese Oxy-fluorides, Promising Catalysts for Oxygen Evolution Reaction under Acidic Media. *Acs Applied Energy Materials* **2021**, *4* (2), 1173−1181.
(22) Pan, S. J.; Li, H.; Liu, D.; Huang, R.; Pan, X. L.; Ren, D.; Li, J.; Shakouri, M.; Zhang, Q. X.; Wang, M. J.; Wei, C. C.; Mai, L. Q.; Zhang, B.; Zhao, Y.; Wang, Z. B.; Graetzel, M.; Zhang, X. D. Efficient and stable noble-metal-free catalyst for acidic water oxidation. *Nat. Commun.* **2022**, *13* (1), 2294.
(23) Peng, J. Y.; Giordano, L.; Davenport, T. C.; Shao-Horn, Y. Stability Design Principles of Manganese-Based Oxides in Acid. *Chem. Mater.* **2022**, *34* (17), 7774−7787.
(24) Euzen, P.; Leone, P.; Mansot, J. L.; Bonneau, P.; Palvadeau, P.; Queignec, M. Synthesis and Structural Studies of Manganese Oxyhalides with a Multisite Framework 0.2. Mn7.5o10br3, a New Lacunar Oxybromide. *Mater. Res. Bull.* **1992**, *27* (12), 1423−1430.
(25) Leone, P.; Euzen, P.; Palvadeau, P. Investigations by magnetic measurements and neutron diffraction studies of the magnetic ordering of Mn8O10Cl3. *J. Magn. Magn. Mater.* **1997**, *172* (1−2), 153−164.
(26) Euzen, P.; Palvadeau, P.; Queignec, M.; Rouxel, J. Preparation and Characterization of the Mixed Oxychloride Femn7o10cl3. *Cr. Acad. Sci. Ii.* **1991**, *312* (4), 367−372.
(27) Fan, Z.; Ji, Y.; Shao, Q.; Geng, S.; Zhu, W.; Liu, Y.; Liao, F.; Hu, Z.; Chang, Y.-C.; Pao, C.-W.; Li, Y.; Kang, Z.; Shao, M. Extraordinary acidic oxygen evolution on new phase 3R-iridium oxide. *Joule* **2021**, *5* (12), 3221−3234.
(28) Wu, H.; Wang, Y.; Shi, Z.; Han, D.; Yang, J.; Wang, P.; Ni, J.; Xiao, M.; Liu, C.; Xing, W. Improving the Lattice Oxygen Reactivity of Rutile IrO2 via Partial Sn Substitution for Acidic Water Oxidation. *J. Phys. Chem. C* **2023**, *127* (26), 12541−12547.
(29) Vesborg, P. C. K.; Jaramillo, T. F. Addressing the terawatt challenge: scalability in the supply of chemical elements for renewable energy. *RSC Adv.* **2012**, *2* (21), 7933−7947.
(30) Cherevko, S. Stabilization of non-noble metal electrocatalysts for acidic oxygen evolution reaction. *Current Opinion in Electrochemistry* **2023**, *38*, No. 101213.
(31) Gao, J.; Tao, H.; Liu, B. Progress of Nonprecious-Metal-Based Electrocatalysts for Oxygen Evolution in Acidic Media. *Adv. Mater.* **2021**, *33* (31), No. 2003786.
(32) Geiger, S.; Kasian, O.; Ledendecker, M.; Pizzutilo, E.; Mingers, A. M.; Fu, W. T.; Diaz-Morales, O.; Li, Z.; Oellers, T.; Fruchter, L.; Ludwig, A.; Mayrhofer, K. J. J.; Koper, M. T. M.; Cherevko, S. The stability number as a metric for electrocatalyst stability benchmarking. *Nature Catalysis* **2018**, *1* (7), 508−515.
(33) Edgington, J.; Seitz, L. C. Advancing the Rigor and Reproducibility of Electrocatalyst Stability Benchmarking and Intrinsic Material Degradation Analysis for Water Oxidation. *ACS Catal.* **2023**, *13*, 3379−3394.
(34) Li, A.; Ooka, H.; Bonnet, N.; Hayashi, T.; Sun, Y.; Jiang, Q.; Li, C.; Han, H.; Nakamura, R. Stable Potential Windows for Long-Term Electrocatalysis by Manganese Oxides Under Acidic Conditions. *Angew. Chem., Int. Ed. Engl.* **2019**, *58* (15), 5054−5058.
(35) Takashima, T.; Hashimoto, K.; Nakamura, R. Mechanisms of pH-Dependent Activity for Water Oxidation to Molecular Oxygen by MnO2 Electrocatalyst. *J. Am. Chem. Soc.* **2012**, *134* (3), 1519−1527.
(36) Yamashita, T.; Hayes, P. Analysis of XPS spectra of Fe2+ and Fe3+ ions in oxide materials. *Appl. Surf. Sci.* **2008**, *254* (8), 2441−2449.
(37) Seitz, L. C.; Hersbach, T. J. P.; Nordlund, D.; Jaramillo, T. F. Enhancement Effect of Noble Metals on Manganese Oxide for the Oxygen Evolution Reaction. *J. Phys. Chem. Lett.* **2015**, *6* (20), 4178−4183.
(38) Wilke, M.; Farges, F.; Petit, P.-E.; Brown, G. E.; Martin, F. Oxidation state and coordination of Fe in minerals: An Fe K-XANES spectroscopic study. *Am. Mineral.* **2001**, *86* (5−6), 714−730.
(39) Husain, H.; Hariyanto, B.; Sulthonul, M.; Thamatkeng, P.; Pratapa, S. Local structure examination of mineral-derived Fe2O3 powder by Fe K-edge EXAFS and XANES. *Iop Conf Ser-Mat Sci.* **2018**, *367*, No. 012027.

https://doi.org/10.1021/acs.chemmater.3c02362
Chem. Mater. 2024, 36, 1299−1307